Compact fiber-coupled three degree-of-freedom displacement interferometry for nanopositioning stage calibration

S R Gillmer[1], R C G Smith[2]‡, S C Woody[3], and J D Ellis[1,2]

[1] Department of Mechanical Engineering, University of Rochester, Rochester, NY USA 14627

[2] The Institute of Optics, University of Rochester, Rochester, NY USA 14627

[3] InSituTec Incorporated, 7140 Weddington Road, Suite 144, Concord, NC USA 28027

E-mail: `steven.gillmer@rochester.edu`

Abstract. Heterodyne displacement interferometry is a widely accepted methodology capable of measuring displacements with sub-nanometer resolution in many applications. We present a compact heterodyne system capable of simultaneously measuring Z-displacement along with changes in pitch and yaw using a single measurement beam incident on a plane mirror target. The interferometer's measurement detector utilizes differential wavefront sensing to decouple and measure these three degrees of freedom. Reliable rotational measurements typically require calibration, however, two analytical models are discussed which predict the readout of rotational scaling factors.

PACS numbers: 06.30.Bp, 06.60.Sx, 07.07.Df, 07.07.Tw, 07.60.Ly, 42.60.By, 42.62.Eh

Submitted to: *Meas. Sci. Technol.*

‡ Present address: Semrock, Inc., 3625 Buffalo Road, Suite 6, Rochester, NY USA 14624

1. Introduction

Heterodyne displacement interferometry is a widely accepted methodology used for high resolution optical metrology [1, 2, 3]. Optical heterodyne interferometers are typically capable of measurements with sub-nanometer resolution and nanometer-level uncertainty, that is, if the proper precautions are taken to ensure a confined environment and if a sufficiently frequency stabilized source is used [4, 5]. Although these levels of resolution in translational motion are readily achievable, limitations still exist in the measurement and calibration of multiple degrees of freedom. Commercial interferometers generally only monitor one or at most two degrees of freedom during a single measurement, and in doing so they typically utilize multiple interferometers and multiple retroreflectors or interferometer architectures with multiple passes that require a larger target to accommodate laser spots.

The limitations for simultaneous calibrations are further exacerbated for nanopositioning systems, such as the system shown in Figure 1. Nanopositioning systems are typically piezoelectric driven stages that exhibit 10's to 100's of micrometers of motion with nanometer level or lower minimal step sizes. In many stages, the nanopositioning system has an embedded sensor used for feedback control that is typically calibrated with a laser interferometry system. Using larger retroreflector(s) for linear and angular measurements or large mirrors to accommodate multiple measurement spots on a target can adversely affect the calibration of the nanopositioning system. Most notably, errors can occur in dynamic measurements where the mass of the target lowers the natural frequency considerably and introduces static offsets [6]. Also, offsets between the internal measurement axis and the calibration axis or functional point in the system can cause Abbé errors [7].

In this work, we address these deficiencies by developing a compact interferometer

Figure 1. The InSituTec X20 nanopositioning stage used in this work. Calibration was needed at a position above and offset from the internal displacement sensor.

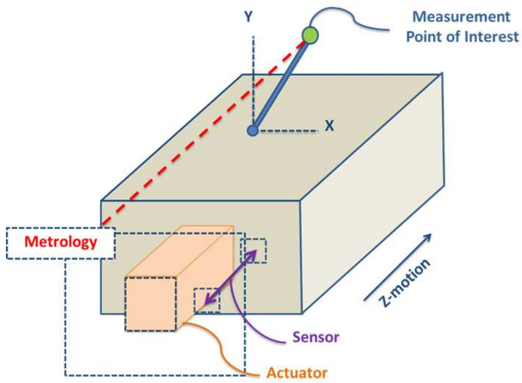

Figure 2. Depending on the application, the calibration may be recorded off-axis, which can introduce Abbé errors if there are rotational motions of the stage. In this work, we can calibrate linear and angular motions of the measurement point of interest with a small target.

capable of measuring three degrees of freedom simultaneously using a single measurement beam incident on a small plane mirror target (<5 mm diameter). The three degrees of freedom measured are the linear displacement along with changes in pitch and yaw. The small target allows for a precise functional point to be known when it does not coincide with the internal measurement axis, as shown in Figure 2. The added angular measurements allow for performing simultaneous coordinate transformations from the functional point to the internal sensor and the small target imparts minimal added mass onto the system.

Other displacement interferometers capable of measuring multiple degrees of freedom simultaneously include the system developed for use in the Laser Interferometer Space Antenna (LISA) [8, 9], the 6-degree of freedom optical sensor for machine tool error characterization [10] and the multi-degree of freedom measuring system developed specifically for coordinate measurement machine error calibrations [11]. The interferometer architecture presented here was developed with a similar design to that used in the LISA project, but has been condensed to a compact size based on Joo-type interferometer architectures [12, 13, 14]. The system is ideal for high resolution calibration because, like other interferometers, it has a high dynamic range, high signal-to-noise ratio, and direct traceability to the meter [15]. In this work, we present an overview of the interferometer, its layout, and working principle. Additionally, we detail how differential wavefront sensing (DWS) is used to measure displacement, pitch, and yaw, including some scaling information for enhancing the sensitivity and we validate this compared to a traditional angle interferometer. We then demonstrate calibration of a nanopositioning stage where the functional point is offset from the internal metrology axis and present data on positioning repeatability and linearity.

The interferometer discussed in this work uses a slightly different approach to measure DWS readout signals. Previously reported DWS technology [8, 9, 16, 17, 18] uses a quadrant photodetector similar to ours, however, all reported results have utilized a beam size much smaller than the quadrant detector active area. Our work incorporates a beam size that is larger than the 2x2 array of photodetectors, thereby simplifying many alignment issues and maximizing signal-to-noise ratio in all four quadrants. Each photodiode in the quadrant photodetector is separated by a small gap that has resulted in non-linearity, crosstalk and drift of the output signals in previous work. Our research has shown that overfilling the detector negates the effects of the small gap because its size is so small compared to the overall beam diameter. Furthermore, when using beams smaller than the overall detector size, spatial variations in photodiode responsivity must be measured and compensated because the measurement beam walks across the detector when the measurement mirror rotates. Overfilling the detector effectively averages these small variations so that spatially varying responsivity becomes negligible – at least in achieving the resolution limits presented in this work.

2. Working Principle

The compact, fiber delivered interferometer can be separated into two different sections – first, the fiber delivered laser source and second, the interferometer architecture and sensors. As shown in Figure 3, light from a stabilized laser source is split equally and each beam is directed towards two acousto-optic modulators (AOMs) which are used to create the heterodyne frequency. The AOMs are driven with slightly different RF signals, ultimately modulating the light to produce interference at that frequency difference. The RF signals used in the experiments for this research were 80.00 MHz and 80.07 MHz, which result in a heterodyne carrier frequency of 70 kHz after interference occurs. After passing through the AOMs, the first order upshifted beams are then both fiber-coupled into polarization maintaining fibers which are prone to mechanical and thermal stress induced phase shifts. The artificial phase shifts, denoted by θ_1 and θ_2, are eventually accounted for by using an optical reference after the fiber launch into the interferometer. Previous research has shown that an optical reference placed after the fiber launch will negate any fiber induced doppler shifts in addition to false frequency modulations

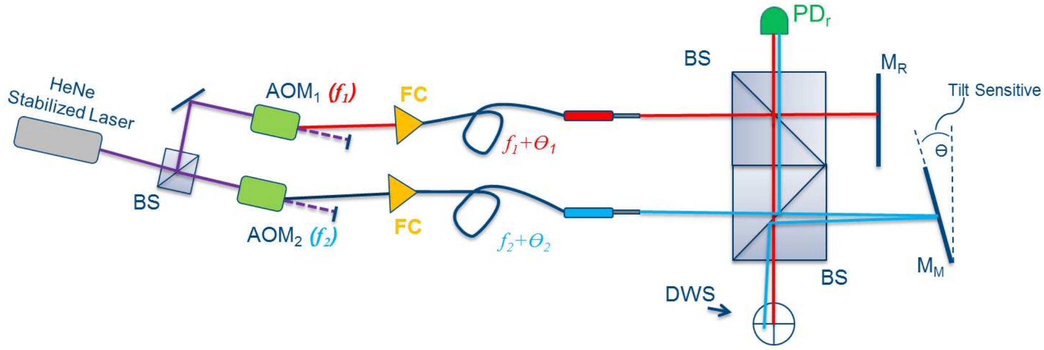

Figure 3. Full schematic of the compact three degree-of-freedom interferometer. (BS: 50/50 non-polarizing beamsplitter, AOM: acousto-optic modulator, FC: fiber coupler, PD: photodetector, M: mirror, DWS: differential wavefront sensing; color online)

which may occur from AOM drifts [14]. It is evident in Figure 3 that the heterodyne frequency is created from the interference of the spatially separated beams from each fiber launch site. Both input beams will have their own associated frequency drift as a result of their individual AOM drifts and PM fiber stress fluctuations, however, once interference occurs artificial frequency drifts from both fiber outputs will be common to both detection sites and thus cancel. Nonetheless, three common fiber perturbations and their impact on the inferferometer were examined. The results of which can be seen in Figure 4 in the time domain and in Figure 5 in the frequency domain. The three perturbations examined were an applied vibration moving the fiber, thermal stressing by breathing on the fibers, and impact loading by tapping on the fibers. The results in Figure 4 show that none of the perturbations significantly affect the noise floor of the interferometer. Furthermore, when examined in the frequency domain, the noise spectra are essentially identical. The frequency domain results were recorded using a 300 Hz low-pass filter which is designated with a dotted line on the figure.

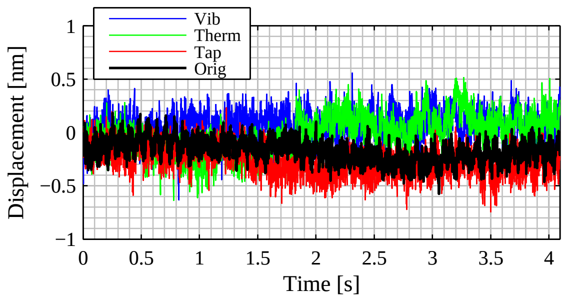

Figure 4. Three common perturbations to polarization maintaining fibers and their effect on interferometric measurements were examined. In the time domain, the noise floor was not significantly affected. (Vib: moving the input fibers, Therm: Thermal excitation by repeatedly breathing on fibers, Tap: Impact loading by repeatedly tapping fibers; color online)

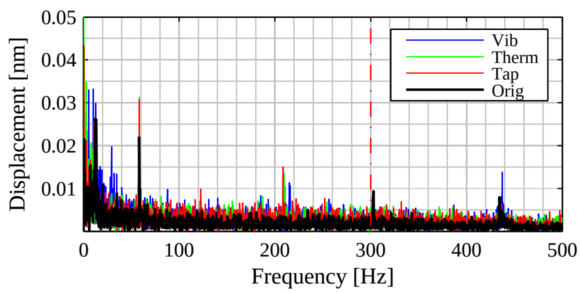

Figure 5. The frequency spectra of three fiber perturbations showed a negligible increase in amplitude of the noise spectra. These results were recorded using a 300 Hz low-pass filter which is designated with a dotted line. (Color online)

Referring to Figure 3, after the two optical beams are collimated into the interferometer and aligned to be parallel, the top beam $(f_1 + \theta_1)$ is split at the top non-polarizing beamsplitter (BS) where 50% of the light transmits and reflects from a reference surface. The reflected light from the reference surface is then reflected at the top BS and interferes with light from bottom BS. Light from the bottom input beam ($f_2 + \theta_2$) is split at the bottom BS and the reflected light is directed to interfere with the $f_1 + \theta_1$ beam that returns form the reference surface in the top BS. This interference signal is detected and is used as the optical reference. Similar to the optical reference, light from the bottom beam ($f_2 + \theta_2$) that is transmitted in the bottom BS is sent to the measurement mirror where it reflects back through the bottom BS and is directed to the quadrant detector. This measurement beam interferes with $f_1 + \theta_1$ light from the top collimator that is reflected in the top BS and transmits through the bottom BS.

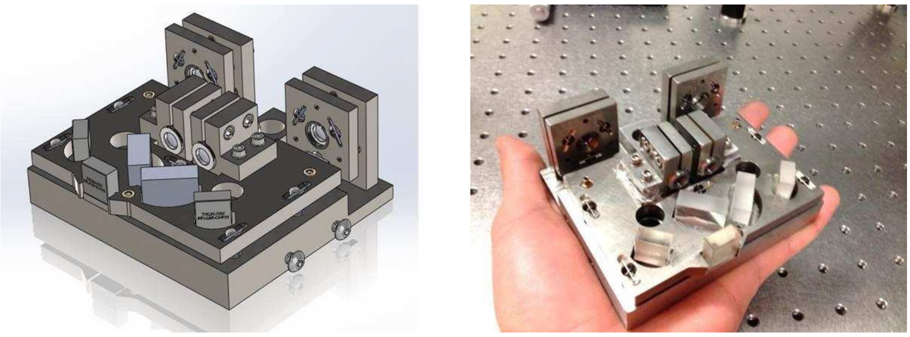

Figure 6. The multi-DOF prototype developed for industrial metrology applications. The interferometer optics are mounted to an invar baseplate to minimize thermal drift.

One of the main differences between the Joo-type architecture and traditional interferometers is the measured phase change is the sum of the optical path length changes for both the reference and measurement arms whereas traditionally it is the difference between measurement and reference optical path lengths. In previous work, this has been exploited to double the measurement resolution. However, modern electronic phase interpolation renders this unnecessary. The Joo-type architecture does allow for compact heterodyne interferometers that need minimal components and no polarizing components. Thus, it is more beneficial to have a short, stable optical path in the reference arm, rather than equalizing the path length to the measurement arm. As shown in Figure 6, the fixed reference surface is mounted to an invar (low thermal expansion material) baseplate, to minimize thermal drift in the interferometer. Wedged fused silica beamsplitters were used to minimize ghost reflections in an effort to eliminate periodic error [19, 20, 21]. Alternatively, as shown in Figure 7, the interferometer can be made into a single optical assembly with the reference surface directly coated on the assembly. Here, anti-reflection coatings are used to minimize ghost reflections and periodic error.

The compact interferometer utilizes differential wavefront sensing (DWS) to measure target mirror displacement and changes in pitch and yaw. The technique uses a quadrant detector to measure four spatially separated interference signals within a single optical interference beam. Based on the geometry of the detector and the interference

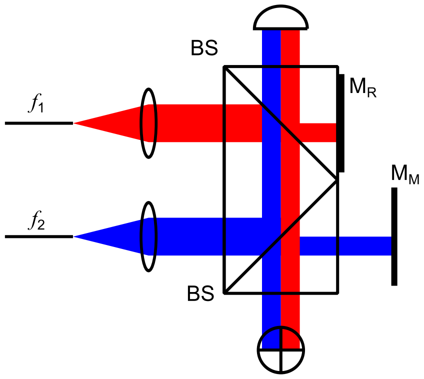

Figure 7. A schematic of the compact 3-DOF interferometer using a single interferometer optic and coating as the reference mirror surface. (Beams are split and offset for clarity.)

phase in each quadrant, the displacement and changes in target pitch and yaw can be decoupled and measured. The concept of DWS is a relatively new technology with a growing variety of applications, mainly in the area of optical alignment [22, 23, 24, 25]. The LISA team expanded DWS for a three degree-of-freedom metrology package that has been extensively outlined and characterized [16, 17, 18] including the performance of a custom phasemeter [26, 27]. Figure 8 provides insight into the operating principal of DWS while Equation 1 describes the required post-processing for three degree-of-freedom measurements.

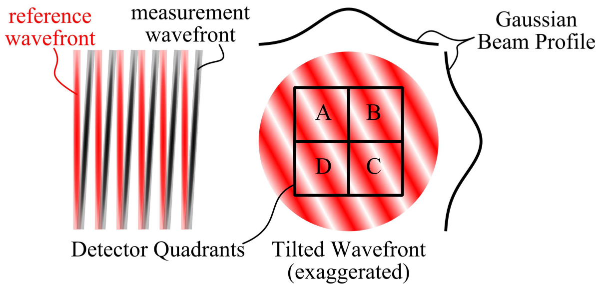

Figure 8. A schematic of a rectangular quadrant photodiode used for differential wavefront sensing with incident tilted interfering wavefronts. The quadrants are labeled A through D. To accurately predict the readout of rotational signals, the Gaussian profiles of interfering beams must be considered as will be discussed later.

The quadrant detector which records DWS signals outputs irradiance values from a 2x2 photodetector array which are then post-processed. Pitch and yaw measurements are obtained using weighted phase averages over symmetrically adjacent pairings of detector elements while overall displacement is a result of the total average phase over all four detectors. The three values are

$$z_d \propto \frac{\phi_A + \phi_B + \phi_C + \phi_D}{4} \tag{1}$$

$$Pitch \propto \frac{(\phi_A + \phi_B) - (\phi_C + \phi_D)}{\Gamma_P} \tag{2}$$

$$Yaw \propto \frac{(\phi_A + \phi_D) - (\phi_B + \phi_C)}{\Gamma_Y}, \tag{3}$$

where ϕ represents detected phase of quadrant A, B, C, or D (see Figure 8), and Γ_P and Γ_Y represent a scaling factor in pitch and yaw measurements that is primarily dependent on beam size, detector size, and beam wavefront.

3. Differential Wavefront Sensing

For rotational measurements, an accurate prediction of the scaling factors designated by Γ_P and Γ_Y in Equations 2 and 3 is not trivial. The Gaussian nature of both interfering beams must be considered to predict accurate results. Hechenblaikner [28] demonstrated an analytical model that can be used to simulate the DWS signals which were cross-calibrations against a commercial hexapod tip/tilt system to within 10% error [18]. The model presented by Hechenblaikner assumes the incident interfering beams are much smaller than the overall size of the quadrant detector. The predicted coupling parameter relating DWS readout to the actual physical rotation taking place, ϕ, is given by

$$D_\phi = \frac{d(DWS_\phi)}{d\phi} = \sqrt{2\pi}\frac{4\omega_{eff}}{\lambda}(1 - \frac{z_{tm}}{R_m})F(\sigma), \tag{4}$$

where ω_{eff} is the effective beam waist related to measurement and reference beam waists by $2/\omega_{eff}^2 = 1/\omega_m^2 + 1/\omega_r^2$, λ is the interferometer wavelength, z_{tm} is the lever-arm length which represents a small translation in relative positions between the measurement and reference beams when the measurement mirror rotates, R_m is the measurement beam curvature and $F(\sigma)$ is given by

$$F(\sigma) = \frac{1}{\sqrt{2}}\sqrt{\frac{1 + \sqrt{1 + \sigma^2}}{1 + \sigma^2}}. \tag{5}$$

The $F(\sigma)$ term depends on a nonlinearity parameter, σ, which is dependent on the beam diameter and relative wavefront curvature of the interfering beams and is given by

$$\sigma = \frac{k\omega_{eff}^2}{4R_{rel}}. \tag{6}$$

In Equation 6, R_{rel} is related to the radii of the reference and measurement beams by $1/R_{rel} = 1/R_r - 1/R_m$ and $k = 2\pi/\lambda$ is the wavenumber. Refer to [28] for a full derivation of the analytical expression. The alternative method for analytical DWS calibration predicts rotational scaling using beams of similar size to the quadrant detector [29]. The major difference between these models is that previously, limits of infinity were used for the irradiance integrations (under the assumption that the incident beams are much smaller than the detector and a circular quadrant detector) while we used finite limits of integration to represent only the portion of the interfering beams detected by the quadrant detector active area. Our analytical expression enables the use of beams of similar size to the quadrant detector thereby simplifying alignment and maximizing signal-to-noise ratio in each quadrant. A schematic demonstrating this difference is shown in Figure 9. Furthermore, our expression is generalized to allow the use of a rectangular quadrant detector. Both derivations assume the interfering beams are described by a fundamental-order Gaussian, however we also include the Gouy phase shift. The measurement beams in this model are described by

$$\begin{aligned} E(r) = |E|\frac{\omega_0}{\omega(z)}\exp(-\frac{r^2}{\omega(z)^2} - ik\frac{r^2}{2R(z)} - ikz \\ +i\zeta(z) + i\omega t), \end{aligned} \tag{7}$$

where r is the distance from the origin, $\omega(z)$ is the beam waist, which is defined as the distance from the origin to $1/e$ electric field amplitude or $1/e^2$ intensity, ω_0 is the minimum beam waist (defined as $\omega(0)$), $R(z)$ is the radius of curvature of the wavefront, and $\zeta(z)$ is the Gouy phase shift. These Gaussian parameters are

$$\begin{aligned} \omega(z) &= \omega_0\sqrt{\left(1+\left(\frac{z}{z_R}\right)^2\right)}, \\ R(z) &= z\left[1+\left(\frac{z_R}{z}\right)^2\right], \quad \text{and} \\ \zeta(z) &= \arctan\left(\frac{z}{z_R}\right), \end{aligned} \tag{8}$$

where z_R is the Rayleigh range

$$z_R = \frac{\pi\omega_0^2}{\lambda}. \tag{9}$$

The two interfering beams are incident on the quadrant photodetector and the total electric field is the sum of the electric fields of the two Gaussian beams. The intensity is proportional to the modulus squared of that electric field. Finally, the result is integrated

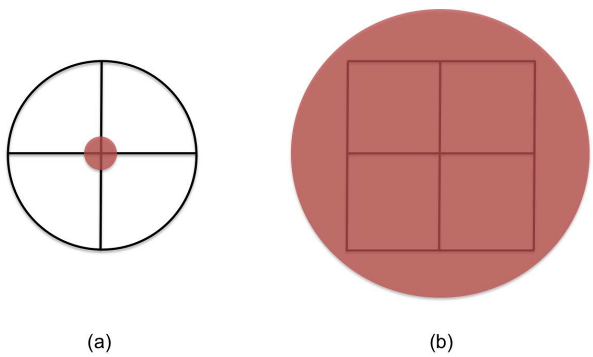

Figure 9. A schematic demonstrating the nominal aspect ratios of beam to quadrant detector used by (a) Hechenblaikner [28] and (b) our model. Overfilling the detector simplifies alignment, maximizes signal-to-noise ratio in each quadrant, and creates a negligible contribution from the gap between detector elements.

over the finite limits of the quadrant detector to determine the optical power on each of the four quadrants. In order to use the previously reported analytical model[28] it was critical to match the wavefronts meticulously in terms of angular and spatial alignment. Our expression has been generalized to take into account the centroid offsets from the center of the quadrant photodetector (δ_x and δ_y) to simplify alignment procedures. Furthermore, since a measured rotation will result in a translation of the measurement beam accross the quadrant detector, our model decouples this result using $\delta x_2 = x_{0,2} + 2\beta z_{m,d}$ and $\delta y_2 = y_{0,2} + 2\alpha z_{m,d}$ where β represents yaw of the measurement mirror and α represents a pitch motion of the measurment mirror. In these expressions $x_{0,2}$ is the initial misalignment along the X-axis of the centroid of the measurement beam, $y_{0,2}$ is the initial misalignment along the Y-axis of the centroid of measurement beam, and $z_{m,d}$ is the distance from the measurement mirror to the detector. Due to the length and complexity of such a general expression, it has been consigned to Appendix A.

Numerical simulations performed using our model demonstrate a significant scaling dependence on beam waist. These simulations can be seen in Figure 10. Additionally, the model predicts that the system will lose sensitivity with any beam waist at mirror rotations close to ≈ 100 μrad. Although the measurements made by this system are not linear, for smaller rotation angles they can be approximated as linear. The results of Figure 10 assumes a square quadrant detector with a width and height of 2.5 mm, however, the model is also heavily dependent on detector size. Figure 11 shows varying effective lengths (the Γ terms in Equations 2 and 3) as a function of beam waist and detector size. Using our model, we compared our 3-DOF measurements against an industry standard angle interferometry system [30] by measuring the same micrometer rotation stage from opposite ends, one such representative result is shown in Figure 12.

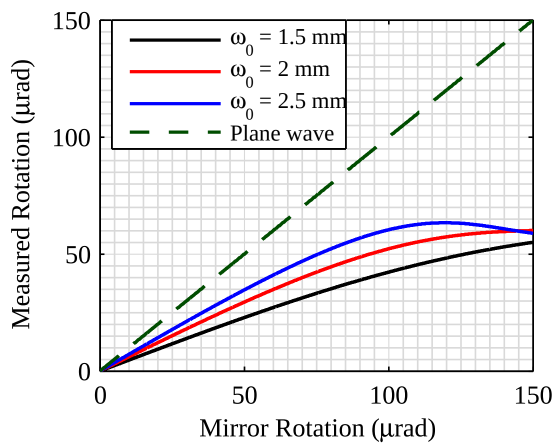

Figure 10. A simulation of the signal measured by our interferometer at several beam waists. The three beam waists result in a different scaling of the measured rotation. All three also lose sensitivity at larger rotation angles, with the largest oscillating as the angle increases (color online).

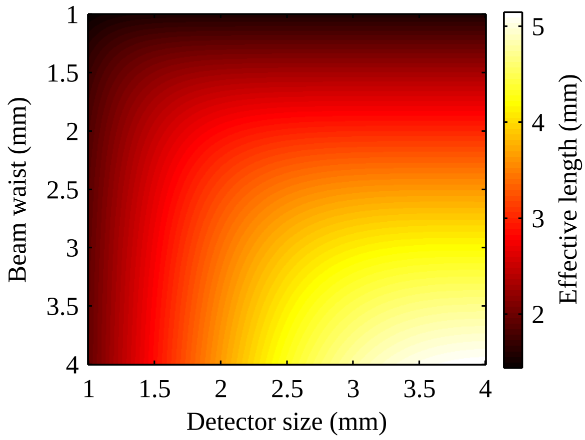

Figure 11. A map of the effective length of a differential wavefront interferometer designed with a range of detector sizes and beam waists. This length determines the denominator terms in Equations 2 and 3 (color online).

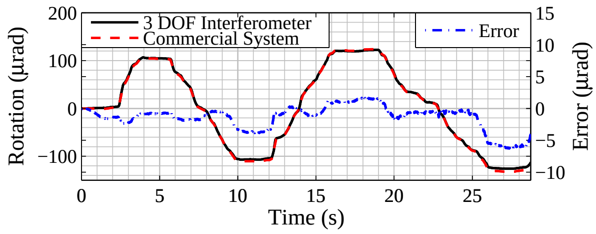

Figure 12. Using the analytical model proposed in [29], rotational scaling was predicted to within 5% error over the full measurement range when compared against an industry standard angle interferometer. (Color online)

The beam waists and the wavefront curvatures of the measurement and reference beams were measured with a Shack-Hartmann wavefront sensor with a $\lambda/50$ rms wavefront sensitivity and used in our model to derive expressions for Γ_P and Γ_Y from Equations 2 and 3. Using this model, the results of our angular sensitivity agree with the commercial angle interferometer to approximately 5% over the full measurement range, which is a 50% improvement over previously reported results using DWS. In practice, we are limited by the air currents passing through uncommon optical paths that cause refractive index errors. Typical shopfloor refractive index variations are approximately $1{\times}10^{-7}$ and since both interferometers were measuring the same stage from approximately 100 mm away, the result is approximately 10 nm (100 mm $\times$ 10^{-7} = 10 nm) of error for each interferometer. When dividing by millimeter-scale Γ values in Equations 2 and 3, 10 nm of displacement error is amplified to single microradian levels in rotational measurements (i.e. rotational refractive index error = 10 nm/2.5 mm $\approx$ 4 μrad, assuming a Γ value of 2.5 mm in Equations 2 and 3). Thus, the fluctuations of error in Figure 12 can be reasonably attributed to refractive index.

4. Experimental Results

Figure 14 shows preliminary results of the calibration of the InSituTec X20 stage where the functional point is off axis from the internal capacitance-based displacement sensor, as previously shown in Figure 2. The purpose of calibrating at this location is because this is the desired function point where the systems should be calibrated based on a customer specification. The internal capacitance sensor will be used for closed loop control relative to that point.

The quadrant detector used for all measurements in this paper was made by Electro-Optical Systems, Inc. (part number S-025-QUAD-E4/1MHz). The detector has a 2.5 mm × 2.5 mm overall active area with a gap size of less than 0.050 mm between detector elements and a Noise Equivalent Power (NEP) of less than 1.5×10^{-12} W/Hz$^{1/2}$. The responsivities of all four detectors were assumed equal. Our AOMs were made by Isomet Corporation (model number 1250C with model number 522C-2 digital modulation RF drivers). The AOMs were driven at 80.00 MHz and 80.07 MHz creating a nominal heterodyne frequency of 70 kHz once interference occurs. Our data acquisition unit was a custom FPGA-based phasemeter sold by InSituTec, Inc. connected to the host PC through USB. The noise floor of the system is shown in Figure 13 and was obtained by sampling at 100 kHz and applying a low-pass filter of 300 Hz.

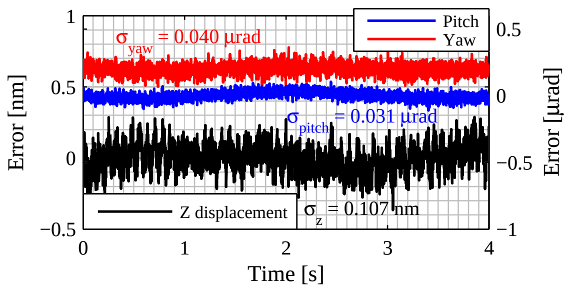

Figure 13. Noise floor measurements using the custom FPGA-based phasemeter developed by InSituTec, Inc. with a 300 Hz low-pass filter implemented. Stage was held at a constant voltage. Data axes have been offset for clarity. (Color online)

The stage was displaced using a slow sine wave under open loop control where the pitch and yaw was monitored simultaneously. The pitch and yaw values are estimated based on the nominal beam size and detector geometry. The interferometer's measured linear displacement of the target was in good agreement with the internal capacitance sensor within the piezo stage. Figure 15 shows the deviation between the two sensors. The two sensors were linear to within 130 nm pk-pk, which was repeatable. This deviation between the sensors was used in a custom linearization algorithm. After applying the algorithm, the stage is capable of holding to within 4.7 nm pk-pk over the range of the stage. Fitting the error to a low order polynomial results in negligible non-linearity.

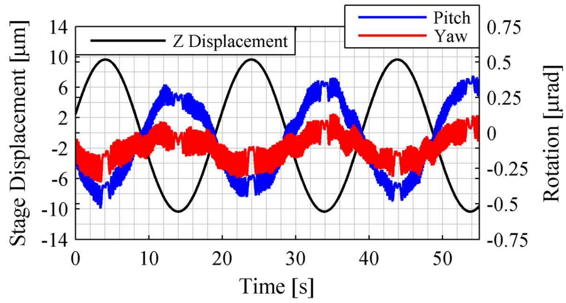

Figure 14. Preliminary testing of the 3-DOF interferometer at the X20 functional point. The X20 nanopositioning stage was operated in open loop using a sinusoidal voltage input and the corresponding displacement and rotational errors were recorded. (Color online)

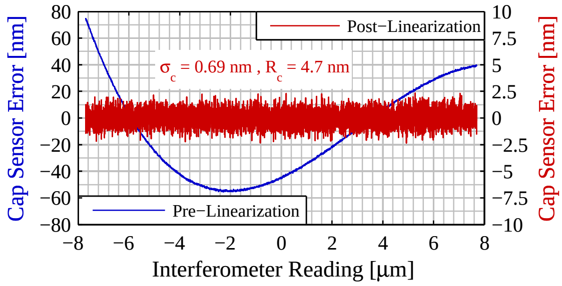

Figure 15. Deviation between the internal capacitance sensor and the external custom interferometer offset from the capacitance sensor measurement axis. The deviation between the two was 130 nm pk-pk, which was reduced to 4.7 nm pk-pk after applying a linearization algorithm. (Color online)

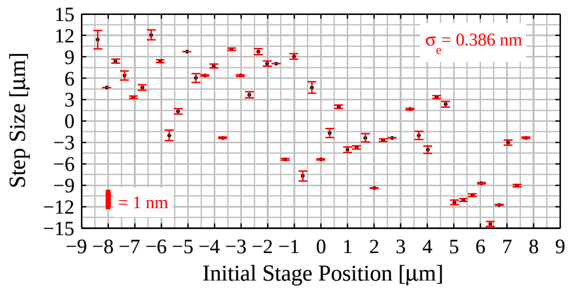

Figure 16. Error after settling for 50 random steps of varying sizes and varying locations throughout the work volume of the X20 stage. The x-axis designates the initial starting position of the stage while the y-axis designates the controlled step size from that initial location. Red error bars represent the standard deviation of the error between the interferometer and internal sensor. The average of the error deviations is less than 0.4 nm over all 50 random steps.

The rotational results in Figure 14 appear noisy because of a phenomenon known as Periodic Nonlinearity (PNL) which is amplified with the use of Equations 2 and 3.

Periodic Nonlinearity (or periodic error) is a well-known phenomenon in displacement interferometry applications. Under the effects of PNL, a nonlinearity with a periodicity of one cycle per 2π change in optical path length is superimposed on top of the ideally linear output. In its simplest principles, PNL is a consequence of signal cross-talk between different frequencies of linearly polarized beams – thereby resulting in parasitic signals. Our developed interferometer has a nominal PNL level of 1 nm pk-pk in translational measurements as a result of ghost reflections in the system. To show how this effect is amplified we will assume a typical Γ value in Equations 2 and 3 of 2.5 mm. If each of the four phase readings has a 1 nm amplitude of PNL, this is amplified to microradian levels by dividing by a millimeter scale denominator (i.e. PNL rotation error = 1 nm/2.5 mm = 0.4 μm). For calibration purposes, this error can be removed by calibrating over the full range and using the slope of the calibration line as shown in Figure 17.

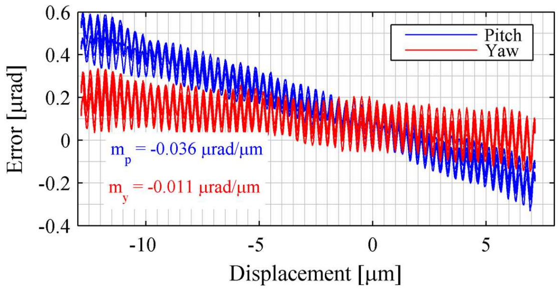

Figure 17. When plotting rotation as a function of stage displacement, the effects of amplified Periodic Nonlinearity in the measured phase are evident. For calibration purposes, this parasitic effect can be removed by calibrating over the full range and using the slope of the calibration line. The y-axis is denoted as error to represent unintended rotations of a stage during translation. (Color online)

Another calibration procedure performed on the stage using the displacement interferometer was a random step test [31]. The stage was commanded to perform 50 random steps of random size within its work volume. The internal capacitance sensor was used to control the stage's motion while the 3-DOF interferometer was used to monitor the performance. The settling algorithm used on the internal capacitance sensor read the current position. If the position remained within a 10 nm displacement window for 50 ms, the stage was deemed "settled" and a trigger signal was sent to the interferometer to record the next 50 ms. The results of this test is shown in Figure 16, where the error bars signify the standard deviation of the error between the interferometer signal and stage position once the stage is deemed settled over the 50 ms window. Based on this test, we can assess the stage's performance to determine work volume and step size bias. Typically, if the linearization algorithm is not performed adequately, larger steps and/or motions occurring at the edge of the work volume can contribute larger areas. Based on these results, no discernable pattern is apparent based on work volume nor step size, and the average standard deviation for the 50 steps was less than 0.4 nm.

Our results do not consider RF crosstalk between DWS readout signals because we have used a nominal 70 kHz heterodyne carrier frequency for all presented measurements. If a larger heterodyne frequency is to be used to discern higher doppler shifts, RF crosstalk becomes more of an issue in the MHz regime. Furthermore, we have also assumed that all four detector elements have the same responsivity, this has proven to be a valid assumption given the agreement between our interferometer and an industry standard angle interferometer. Thermal drift will affect long-term measurements, however, all reported results were conducted over short time-frames thereby negating this effect as much as possible.

5. Conclusions

In summary, we have presented a compact three degree-of-freedom displacement interferometer capable of the simultaneous measurement of Z-displacement and changes in pitch and yaw of a translating nanopositioning stage. The implementation of a novel architecture has significantly reduced the metrology footprint of our interferometer compared to its LISA predecessor. To achieve reliable rotational measurements, the interferometer must be calibrated either against an additional metology tool or through the analytical prediction of scaled DWS readout signals. If the readout signals are to be analytically predicted, two methods have been proposed, one of which was implemented with this interferometer to within 5% error over the full measurement range.

Using this 3-DOF interferometer we demonstrate calibration of a compact, single axis nanopositioning system. After linearization, the capacitance sensor noise was 4.7 nm pk-pk over the full range with a standard deviation of less than 0.7 nm. Considering the step size variation from Figure 16, we can conclude we are able to use this interferometer to linearize the stage to within 0.003% (0.4 nm over a 15.4 m range). A random step test was then performed, demonstrating no work volume or step size bias between the internal capacitance sensor and 3-DOF interferometer. The proposed 3-DOF interferometer demonstrates that accurate, repeatable calibrations of nanopositioning stages can be performed at a functional point off axis from their internal feedback sensor.

Appendix A

The most reliable and straightforward way to use this 3-DOF interferometer is to calibrate the rotational readout signals to an external metrology tool. After doing so, if the quadrant detector is held in place relative to the interferometer, accurate rotational measurements can be obtained. However, if one wants to predict the rotational scaling, a physical optics simulation can be used to achieve moderately accurate results as seen in Figure 12. In order to do this, the Gaussian nature of the interfering beams must be considered. Even though this Gaussian profile should be used for the reference beams, in practice the photodetector is placed close enough to the center and the unintentional rotation is small enough that a plane wave approximation for the reference signal is valid. The two interfering beams – governed by equation 7 – are incident on the quadrant photodetector and the total electric field given on the detector is the sum of the electric fields of the two beams, E_1 and E_2. The irradiance is proportional to the modulus squared of this electric field,

$$\begin{aligned}
I(x,y) \propto\ & A_1^2 \exp\Big\{-2\frac{(x-\delta x_1)^2+(y-\delta y_1)^2}{\omega(z_1)^2}\Big\} \\
&+ A_2^2 \exp\Big\{-2\frac{(x-\delta x_2)^2+(y-\delta y_2)^2}{\omega(z_2)^2}\Big\} \\
&+ A_1 A_2 \exp\Big\{-\Big[(x-\delta x_1)^2+(y-\delta y_1)^2\Big]\Big(\frac{1}{\omega(z_1)^2}+\frac{ik}{2R(z_1)}\Big)\Big\} \\
&* \exp\Big\{-\Big[(x-\delta x_2)^2+(y-\delta y_2)^2\Big] * \left(\frac{1}{\omega(z_2)^2}-\frac{ik}{2R(z_2)}\right)\Big\} \\
&* \exp\left[i(\zeta(z_1)-\zeta(z_2))\right] * \exp\left\{ik\left[2\beta(x-\delta x_2)\right.\right. \\
&* \left.\left. +2\alpha(y-\delta y_2)+\omega_s t-\phi_m\right\} + \text{c.c.}
\end{aligned} \tag{A.1}$$

where the majority of terms have been defined in Section 3, c.c. denotes the complex conjugate, $A_1 = |E_1|\omega_{0,1}/\omega(z_1)$, $A_2 = |E_2|\omega_{0,2}/\omega(z_2)$, δx_1 is the distance along the X-axis between the detector center and the centroid of the first beam, δy_1 is the distance along the Y-axis between the detector center and the centroid of the first beam, and δx_2 and δy_2 are the same for the second beam. These distances are $\delta x_1 = x_{0,1}$, $\delta y_1 = y_{0,1}$, $\delta x_2 = x_{0,2} + 2\beta z_{m,d}$, and $\delta y_2 = y_{0,2} + 2\alpha z_{m,d}$. For these parameters, $x_{0,1}$ is the initial misalignment along the X-axis of the centroid of E_1, $y_{0,1}$ is the initial misalignment along the Y-axis of the centroid of E_1, $x_{0,2}$ and $y_{0,2}$ are the same for E_2, and $z_{m,d}$ is the distance from the measurement mirror to the detector. As before, the irradiance must be integrated over the detector area to determine the measured signal on each detector. Equation A.1 can be integrated over the finite limits of the detector where the resulting optical power on the A quadrant is

$$
\begin{aligned}
A \propto &\int_0^w \int_0^h I(x,y)\mathrm{d}x\mathrm{d}y = \\
&\mathrm{D.C.} + \frac{A_1 A_2}{2}\sqrt{\frac{\pi}{\frac{1}{\omega(z_1)^2}+\frac{1}{\omega(z_2)^2}+\frac{ik}{2R(z_1)}-\frac{ik}{2R(z_2)}}} \\
&* \exp\left[-\left(\frac{1}{\omega(z_1)^2}+\frac{ik}{2R(z_1)}\right)\left(\delta x_1^2+\delta y_1^2\right)\right. \\
&\left.-\left(\frac{1}{\omega(z_2)^2}-\frac{ik}{2R(z_2)}\right)\left(\delta x_2^2+\delta y_2^2\right)\right] \\
&* \exp\left[i\left(\zeta(z_1)-\zeta(z_2)+\omega_s t-\phi_m-2k\beta\delta x_2-2k\alpha\delta y_2\right)\right] \\
&* \exp\left\{\frac{\left[ik\beta+\left(\frac{1}{\omega(z_1)^2}+\frac{ik}{2R(z_1)}\right)\delta x_1+\left(\frac{1}{\omega(z_2)^2}-\frac{ik}{2R(z_2)}\right)\delta x_2\right]^2}{\frac{1}{\omega(z_1)^2}+\frac{1}{\omega(z_2)^2}+\frac{ik}{2R(z_1)}-\frac{ik}{2R(z_2)}}\right\} \\
&* \left[\sqrt{\frac{1}{\omega(z_1)^2}+\frac{1}{\omega(z_2)^2}+\frac{ik}{2R(z_1)}-\frac{ik}{2R(z_2)}}x\right. \\
&\left.\left.+\frac{ik\beta+\left(\frac{1}{\omega(z_1)^2}+\frac{ik}{2R(z_1)}\right)\delta x_1+\left(\frac{1}{\omega(z_2)^2}-\frac{ik}{2R(z_2)}\right)\delta x_2}{\sqrt{\frac{1}{\omega(z_1)^2}+\frac{1}{\omega(z_2)^2}+\frac{ik}{2R(z_1)}-\frac{ik}{2R(z_2)}}}\right]\right|_0^w \\
&* \exp\left\{\frac{\left[ik\alpha+\left(\frac{1}{\omega(z_1)^2}+\frac{ik}{2R(z_1)}\right)\delta y_1+\left(\frac{1}{\omega(z_2)^2}-\frac{ik}{2R(z_2)}\right)\delta y_2\right]^2}{\frac{1}{\omega(z_1)^2}+\frac{1}{\omega(z_2)^2}+\frac{ik}{2R(z_1)}-\frac{ik}{2R(z_2)}}\right\} \\
&* \left[\sqrt{\frac{1}{\omega(z_1)^2}+\frac{1}{\omega(z_2)^2}+\frac{ik}{2R(z_1)}-\frac{ik}{2R(z_2)}}y\right. \\
&\left.\left.+\frac{ik\alpha+\left(\frac{1}{\omega(z_1)^2}+\frac{ik}{2R(z_1)}\right)\delta y_1+\left(\frac{1}{\omega(z_2)^2}-\frac{ik}{2R(z_2)}\right)\delta y_2}{\sqrt{\frac{1}{\omega(z_1)^2}+\frac{1}{\omega(z_2)^2}+\frac{ik}{2R(z_1)}-\frac{ik}{2R(z_2)}}}\right]\right|_0^h + \mathrm{c.c.}
\end{aligned} \tag{A.2}
$$

Similarly, the power on the other three quadrants is given simply by changing the limits of integration according to

$$
\begin{aligned}
A &\propto \int_0^w \int_0^h I(x,y)\,\mathrm{d}y\mathrm{d}x, \\
B &\propto \int_0^w \int_{-h}^0 I(x,y)\,\mathrm{d}y\mathrm{d}x, \\
C &\propto \int_{-w}^0 \int_{-h}^0 I(x,y)\,\mathrm{d}y\mathrm{d}x, \quad \text{and} \\
D &\propto \int_{-w}^0 \int_0^h I(x,y)\,\mathrm{d}y\mathrm{d}x
\end{aligned}. \tag{A.3}
$$

The full rectangular quadrant detector has a width $2w$ and a height $2h$, thus, these limits of integration are all from the center of all four detectors.

After the D.C. components are filtered out, the signal from one of the quadrants has the form

$$A = f_A(z,\alpha,\beta)e^{i\omega_s t} + f^*(z,\alpha,\beta)e^{-i\omega_s t}. \tag{A.4}$$

The lock-in detection scheme was used in this work to detect phase, thus the in-phase and quadrature components become

$$
\begin{aligned}
I_A &= \frac{1}{2}\left(e^{i\omega_s t} + e^{-i\omega_s t}\right)\left[f_A(z,\alpha,\beta)e^{i\omega_s t} + f^*(z,\alpha,\beta)e^{-i\omega_s t}\right] \quad \text{and} \\
Q_A &= \frac{1}{2}\left(e^{i(\omega_s t+\pi/2)} + e^{-i(\omega_s t+\pi/2)}\right)\left(f_A(z,\alpha,\beta)e^{i\omega_s t} + f^*(z,\alpha,\beta)e^{-i\omega_s t}\right).
\end{aligned} \tag{A.5}
$$

After carrying out this multiplication and removing the signals at $2\omega_s$, the resulting components are

$$
\begin{aligned}
I_A &= \frac{1}{2}\left[f_A(z,\alpha,\beta) + f_A^*(z,\alpha,\beta)\right] \quad \text{and} \\
Q_A &= \frac{i}{2}\left[f_A^*(z,\alpha,\beta) - f_a(z,\alpha,\beta)\right],
\end{aligned} \tag{A.6}
$$

which is equivalent to

$$
\begin{aligned}
I_A &= \Re\left[f_A(z,\alpha,\beta)\right] \quad \text{and} \\
Q_A &= \Im\left[f_A(z,\alpha,\beta)\right].
\end{aligned}
$$

Since the arctangent is computed, the phase is then

$$
\phi_A = \arctan\frac{\Im\left[f_A(z,\alpha,\beta)\right]}{\Re\left[f_A(z,\alpha,\beta)\right]} = \theta_A + m\pi, \tag{A.8}
$$

where ϕ_A is the angle of the complex quantity described by $f_A(z,\alpha,\beta) = |f_A(z,\alpha,\beta)|e^{i\phi_A}$. The remaining three phase terms from the other photodiode quadrants can be determined using a similar procedure. This model was used to simulate the readout of measured rotations (Figures 10 and 11). The predicted effective length in Figure 11 is inserted into Equations 2 and 3 as the Γ terms.

References

[1] S.J. Bennett. *Length and displacement measurement by laser interferometry*, pages 135–159. Applied Science Publishers, 1983.

[2] C.R. Steinmetz. Sub-micron position measurement and control on precision machine tools with laser interferometry. *Precision Engineering*, 12(1):12–24, 1990.

[3] P. Hariharan. *Optical Interferometry*. Academic Press, 2003.

[4] W.T. Estler. High-accuracy displacement interferometry in air. *Applied Optics*, 24(6):808–815, 1985.

[5] Han Haitjema. Achieving traceability and sub-nanometer uncertainty using interferometric techniques. *Measurement Science and Technology*, 19(8), 2008.

[6] J.D. Ellis, S.R. Gillmer, and B. O'Connor. Methods for performance evaluation of single axis positioning systems: dynamic angular performance. In *Proceedings of the 28th ASPE Annual Meeting, St. Paul, MN*, 2013.

[7] J.B. Bryan. The Abbé principle revisited- an updated interpretation. *Precision Engineering*, 1(3):129–132, 1979.

[8] T. Schuldt, M. Gohlke, D. Weise, U. Johann, A. Peters, and C. Braxmaier. Picometer and nanoradian optical heterodyne interferometry for translation and tilt metrology of the LISA gravitational reference sensor. *Classical and Quantum Gravity*, 26(8), 2009.

[9] M. Armano, M. Benedetti, J. Bogenstahl, D. Bortoluzzi, P. Bosetti, N. Brandt, A. Cavalleri, G. Ciani, I. Cristofolini, A.M. Cruise, K. Danzmann, I. Diepholz, G. Dixon, R. Dolesi, J. Fauste, L. Ferraioli, D. Fertin, W. Fichter, M. Freschi, A. García, C. García, A. Grynagier, F. Guzmán, E. Fitzsimons, G. Heinzel, M. Hewitson, D. Hollington, J. Hough, M. Hueller, D. Hoyland, O. Jennrich, B. Johlander, C. Killow, A. Lobo, D. Mance, I. Mateos, P.W. McNamara, A. Monsky, D. Nicolini, D. Nicolodi, N. Nofrarias, M. Perreur-Lloyd, E. Plagnol, G.D. Racca, J. Ramos-Castro, D. Robertson, J. Sanjuan, M.O. Schulte, D.N.A. Shaul, M. Smit, L. Stagnaro, F. Steier, T.J. Sumner, N. Tateo, D. Tombolato, G. Vischer, S. Vitale, G. Wanner, H. Ward, S. Waschke, V. Wand, P. Wass, W.J. Weber, T. Ziegler, and P. Zweifel. LISA pathfinder: the experiment and the route to LISA. *Classical and Quantum Gravity*, 26(9), 2009.

[10] J.J. Kroll. *Six degree of freedom optical sensor for dynamic measurement of linear axes.* PhD thesis, University of North Carolina, Charlotte, 2003.

[11] P.S. Huang J. Ni and S.M. Wu. A multi-degree-of-freedom measuring system for CMM geometric errors. *Journal of Engineering for Industry*, 114:362–369, 1992.

[12] K-N. Joo, J.D. Ellis, J.W. Spronck, P.J.M. van Kan, and R.H. Minnig Schmidt. Simple heterodyne laser interferometer with subnanometer periodic errors. *Optics Letters*, 34(3):386–388, 2009.

[13] K-N. Joo, J.D. Ellis, E.S. Buice, J.W. Spronck, and R.H. Munnig Schmidt. High resolution heterodyne interferometer without detectable periodic nonlinearity. *Optics Express*, 18(2):1159–1165, 2010.

[14] J.D. Ellis, A.J.H. Meskers, J.W. Spronck, and R.H. Munnig Schmidt. Fiber-coupled displacement interferometry without periodic nonlinearity. *Optics Letters*, 36:3584–3586, 2011.

[15] Frank C Demarest. High-resolution, high-speed, low data age uncertainty, heterodyne displacement measuring interferometer electronics. *Measurement Science and Technology*, 9(7):1024–1030, 1998.

[16] G. Heinzel, C. Braxmaier, R. Schilling, A. Rüdiger, D. Robertson, M. te Plate, V. Wand, K. Arai, U. Johann, and K. Danzmann. Interferometry for the LISA technology package (LTP) aboard smart-2. *Classical and Quantum Gravity*, 20(10):S153–S161, 2003.

[17] G. Hechenblaikner, R. Gerndt, U. Johann, P. Luetzow-Wentzky, V. Wand, H. Audley, K. Danzmann, A. Garcia-Marin, G. Heinzel, M. Nofrarias, and F. Steier. Coupling characterization and noise studies of the optical metrology system onboard the LISA pathfinder mission. *Applied Optics*, 49(29):5665–5677, 2010.

[18] D.I. Robertson, E.D. Fitzsimons, C.J. Killow, M. Perreur-Lloyd, H. Ward, J. Bryant, A.M. Cruise, G. Dixon, D. Hoyland, D. Smith, and J. Bogenstahl. Construction and testing of the optical bench for LISA pathfinder. *Classical and Quantum Gravity*, 30(8), 2013.

[19] R. Quenelle. Nonlinearity in interferometer measurements. *Hewlett-Packard Journal*, 34(4):10, 1983.

[20] W. Hou and G. Wilkening. Investigation and compensation of the nonlinearity of heterodyne interferometers. *Precision Engineering*, 14(2):91–98, 1992.

[21] J.M. De Freitas and M.A. Player. Polarization effects in heterodyne interferometry. *Journal of Modern Optics*, 42(9):1875–1899, 1995.

[22] E. Morrison, B.J. Meers, D.I. Robertson, and H. Ward. Experimental demonstration of an automatic alignment system for optical interferometers. *Applied Optics*, 33(22):5037–5040, 1994.

[23] E. Morrison, B.J. Meers, D.I. Robertson, and H. Ward. Automatic alignment of optical interferometers. *Applied Optics*, 33(22):5041–5049, 1994.

[24] H. Grote, G. Heinzel, A. Freise, S. Goßler, B. Willke, H. Lück, H. Ward, M.M. Casey, K.A. Strain, D.I. Robertson, J. Hough, and K. Danzmann. Alignment control of GEO 600. *Classical and Quantum Gravity*, 21(5):S441–S449, 2004.

[25] Holger Müller, Sheng wey Chiow, Quan Long, Christoph Vo, and Steven Chu. Active sub-rayleigh alignment of parallel or antiparallel laser beams. *Opt. Lett.*, 30(24):3323–3325, Dec 2005.

[26] G. Heinzel, V. Wand, A. García, O. Jennrich, C. Braxmaier, D. Robertson, K. Middleton, D. Hoyland, A. Rüdiger, R. Schilling, U. Johann, and K. Danzmann. The LTP interferometer

and phasemeter. *Classical and Quantum Gravity*, 21(5):S581–S587, 2004.

[27] F.G. Cervantes, G. Heinzel, A.F. García Marín, V. Wand, Steier F., O. Jennrich, and Karsten D. Real-time phase-front detector for heterodyne interferometers. *Applied Optics*, 46(21):4541–4548, 2007.

[28] G. Hechenblaikner. Measurement of the absolute wavefront curvature radius in a heterodyne interferometer. *Journal of the Optical Society of America A*, 27(9):2078–2083, 2010.

[29] R.G. Smith. Physical optics analysis of a fiber-delivered displacement interferometer. Master's thesis, University of Rochester, 2012.

[30] Renishaw – ML10 measurement system, cited January 2014.

[31] S. Ludwick. Methods for performance evaluation of single axis positioning systems: move and settle performance. In *Proceedings of the 28th ASPE Annual Meeting, St. Paul, MN*, 2013.